

Article

Nerve Targeting via Myelin Protein Zero and the Impact of Dimerization on Binding Affinity

Nataliia Berehova ¹, Tessa Buckle ¹, Maarten P. van Meerbeek ¹, Anton Bunschoten ², Aldrik H. Velders ² and Fijs W. B. van Leeuwen ^{1,2,*}

¹ Interventional Molecular Imaging Laboratory, Department of Radiology, Leiden University Medical Center, Albinusdreef 2, 2300 RC Leiden, The Netherlands

² Laboratory of BioNanoTechnology, Wageningen University & Research, Bornse Weiland 9, 6708 WG Wageningen, The Netherlands

* Correspondence: f.w.b.van_leeuwen@lumc.nl

Abstract: Background: Surgically induced nerve damage is a common but debilitating side effect. By developing tracers that specifically target the most abundant protein in peripheral myelin, namely myelin protein zero (P0), we intend to support fluorescence-guided nerve-sparing surgery. To that end, we aimed to develop a dimeric tracer that shows a superior affinity for P0. Methods: Following truncation of homotypic P0 protein-based peptide sequences and fluorescence labeling, the lead compound Cy5-P0_{101–125} was selected. Using a bifunctional fluorescent dye, the dimeric Cy5-(P0_{101–125})₂ was created. Assessment of the performance of the mono- and bi-labeled compounds was based on (photo)physical evaluation. This was followed by in vitro assessment in P0 expressing Schwannoma cell cultures by means of fluorescence confocal imaging (specificity, location of binding) and flow cytometry (binding affinity; K_D). Results: Dimerization resulted in a 1.5-fold increase in affinity compared to the mono-labeled counterpart (70.3 ± 10.0 nM vs. 104.9 ± 16.7 nM; $p = 0.003$) which resulted in a 4-fold increase in staining efficiency in P0 expressing Schwannoma cells. Presence of two targeting vectors also improves a pharmacokinetics of labeled compounds by lowering serum binding and optical stability by preventing dye stacking. Conclusions: Dimerization of the nerve-targeting peptide P0_{101–125} proves a valid strategy to improve P0 targeting.

Keywords: fluorescence imaging; nerve targeting; myelin protein zero; fluorescence-guided surgery



Citation: Berehova, N.; Buckle, T.; van Meerbeek, M.P.; Bunschoten, A.; Velders, A.H.; van Leeuwen, F.W.B. Nerve Targeting via Myelin Protein Zero and the Impact of Dimerization on Binding Affinity. *Molecules* **2022**, *27*, 9015. <https://doi.org/10.3390/molecules27249015>

Academic Editor: Haiying Liu

Received: 3 November 2022

Accepted: 13 December 2022

Published: 17 December 2022

Publisher's Note: MDPI stays neutral with regard to jurisdictional claims in published maps and institutional affiliations.



Copyright: © 2022 by the authors. Licensee MDPI, Basel, Switzerland. This article is an open access article distributed under the terms and conditions of the Creative Commons Attribution (CC BY) license (<https://creativecommons.org/licenses/by/4.0/>).

1. Introduction

Accidental surgical damage to nerves can yield debilitating side effects. For example, damage to key sensory nerves (6–22 mm in diameter) during orthopedic surgery may mean limbs lose function [1]. Alternatively, damage caused to small nerves (1–2 mm in diameter) during pelvic surgery can induce incontinence and erectile dysfunction [2–4]. Even when nerve sparing is specifically intended in prostate cancer patients, 30% still suffer from the effects of surgically induced damage [5,6]. Prevention of damage starts with the surgeon's ability to identify nerves residing in the surgical field.

Nerve-specific fluorescence imaging [7] could help increase the specificity and sensitivity of intraoperative nerve identification. To this end different strategies for imaging have been put forward. In general, nerve imaging can be realized via neuronal tracing [8], by targeting the intracellular myelin basic protein (MBP) [9,10] or extracellular myelin protein zero (MPZ or P0) [11,12]. The latter especially provides an interesting imaging target, as it makes up 80% of the myelin protein content (Figure 1A, [11]) and is specific for the peripheral nervous system (PNS). Previous efforts towards the truncation of the extracellular portion of P0, followed by fluorescence labeling, allowed for P0 targeting in vitro and in vivo (mice and porcine models; lead Cy5-P0_{101–125}) [11].

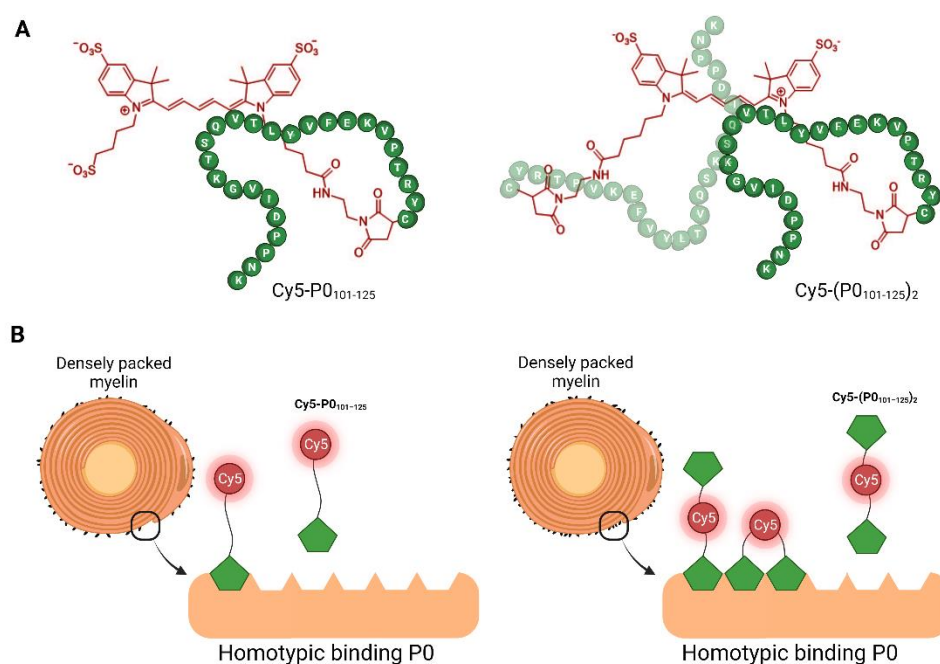


Figure 1. (A) Schematic structure of mono-labeled Cy5-P0₁₀₁₋₁₂₅ and bi-labeled Cy5-(P0₁₀₁₋₁₂₅)₂ agents; (B) dimerization effect on binding affinity of Cy5-P0₁₀₁₋₁₂₅ (left) and Cy5-(P0₁₀₁₋₁₂₅)₂ (right) to Schwann cells.

It is becoming increasingly obvious that signal intensity and signal-to-background ratios play a key role in fluorescent-guided surgery approaches [13]. Increasing the targeting affinity and via that route and enhancing the uptake of the agent is a well-accepted route for improving the signal intensity. A known strategy for affinity enhancement is the exploration of the multivalency concept. This concept is widely studied in the field of supramolecular chemistry [14–16]. Multiple studies also indicate that the multivalency approach also applies to imaging agents [17–22]. At the same time, there is evidence that multimerization of targeting vectors helps to “shield” the imaging agent (fluorescent dye) from the environment, hereby improving the pharmacokinetic properties [23–25].

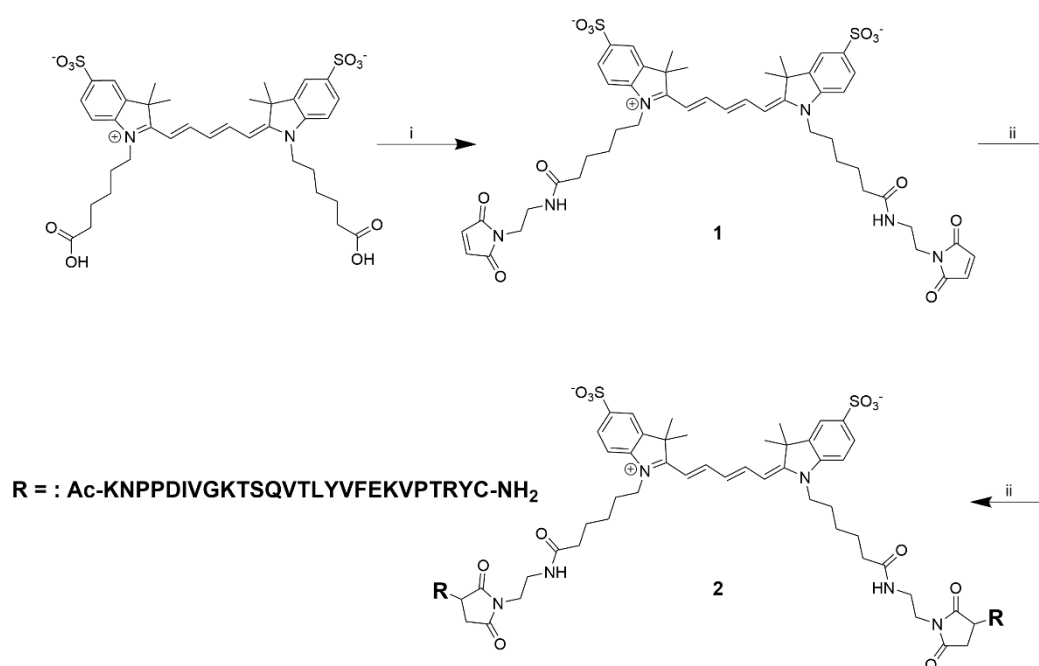
We reasoned that the lead P0₁₀₁₋₁₂₅ peptide would allow us to synthesize a dimeric Cy5-(P0₁₀₁₋₁₂₅)₂ agent with lower serum binding, dye stacking, and superior P0 affinity compared to the monomer, and with that, enhance the signal intensity. Bifunctional constructs containing two thiol-reactive maleimide groups formed the basis of the design for the peptide conjugation [26] (Figure 1).

Following synthesis, compounds were evaluated using NMR and MS. Chemical and photophysical properties were measured and analyzed. Fluorescence intensity and affinity enhancement of the bi-labeled agent were studied *in vitro* (flow cytometry and confocal microscopy) using cultures of P0-expressing Schwannoma cells compared to the parental mono-labeled Cy5-P0₁₀₁₋₁₂₅.

2. Results

2.1. Chemistry

Following a literature procedure [27], we first synthesized COOH-(SO₃)Cy5(SO₃)-COOH. For the maleimide incorporation, the symmetrical COOH-(SO₃)Cy5(SO₃)-COOH was treated with *N*-(2-aminoethyl)maleimide trifluoroacetate salt, *N*-methyl morpholine was used as a base, and PyBOP was used as a coupling agent. Next, Cy5-(P0₁₀₁₋₁₂₅)₂ (2) was synthesized by adding excess of the free peptide P0₁₀₁₋₁₂₅ to Maleimide-(SO₃)Cy5(SO₃)-Maleimide (1) in PBS (Scheme 1).



Scheme 1. Reagents and conditions: (i) *N*-(2-aminoethyl)maleimide trifluoroacetate salt, PyBOP, *N*-methyl morpholine, DMF, r.t., 2 h; (ii) P0_{101–125}, phosphate-buffered saline (pH 7.4), DMF, r.t., 2 h.

2.2. Chemical and Photophysical Properties

Table 1 provides a summary of the chemical and photophysical properties of the protein-conjugated compounds and the corresponding free dyes.

Table 1. Chemo- and photophysical properties of mono-labeled Cy5-P0_{101–125} and bi-labeled Cy5-(P0_{101–125})₂ and corresponding free cyanine dyes.

Property	Sulfonate-(SO ₃)Cy5(SO ₃)-COOH *	Cy5-P0 _{101–125}	COOH-(SO ₃)Cy5(SO ₃)-COOH	Cy5-(P0 _{101–125}) ₂
$\lambda_{\text{ex}}/\lambda_{\text{Em}}$ in H ₂ O/PBS (stokes shift, nm)	648/664 (16)	650/671 (21)	648/667 (19)	654/671 (17)
Brightness (M ⁻¹ cm ⁻¹ in PBS)	53.000	55.660 [†]	46.000	49.242 [†]
Serum protein binding, %	49 ± 8	89 ± 2	70 ± 4	63 ± 3
logP _(o/w)	-1.42 ± 0.00	-1.39 ± 0.09	-1.62 ± 0.01	-0.57 ± 0.01
Net charge	-2	0	-3	+3
Glutathione stability (at 6 h), %	95	92	95	96
Photobleaching, %	93	94	95	71

$\lambda_{\text{ex}}/\lambda_{\text{Em}}$, excitation and emission wavelengths, respectively; PBS, phosphate-buffered saline; * previously reported by Spa et al. [27]; [†] calculated using the molar extinction coefficient of the free dye.

When compared to Cy5-P0_{101–125}, the lipophilicity of Cy5-(P0_{101–125})₂ was shown to be increased, while the degree of serum protein binding decreased by 26% ($p = 0.0002$). The glutathione stability tests only showed 4% degradation for both compounds.

Brightness values for Cy5-P0_{101–125} and Cy5-(P0_{101–125})₂ were comparable (Table 1: $p = 0.3450$). On the other hand, Cy5-(P0_{101–125})₂ showed a slightly lower photostability than its monosubstituted counterpart (Figure 2D; $p = 0.0139$) as well as compared with free dyes (Table 1).

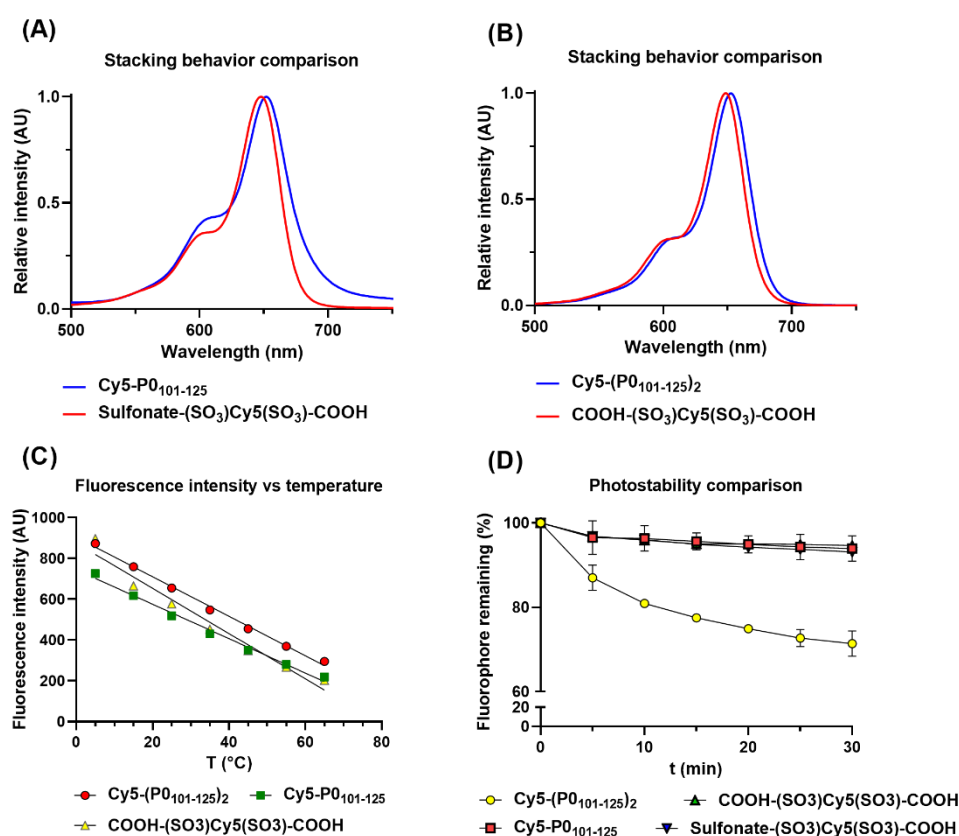


Figure 2. Photophysical properties of Cy5-P0₁₀₁₋₁₂₅ and Cy5-(P0₁₀₁₋₁₂₅)₂. (A) Comparison in stacking behavior between Cy5-P0₁₀₁₋₁₂₅ and corresponding free sulfonate-(SO₃)Cy5((SO₃)-COOH) dye at 8mM measured in water. (B) Comparison in stacking behavior between Cy5-(P0₁₀₁₋₁₂₅)₂ and corresponding free COOH-(SO₃)Cy5(SO₃)-COOH dye at 8 mM measured in water; each spectrum was normalized at its wavelength of maximum absorbance. (C) Fluorescence intensity dependence of the temperature for Cy5-P0₁₀₁₋₁₂₅, Cy5-(P0₁₀₁₋₁₂₅)₂ and symmetrical free dye COOH-(SO₃)Cy5((SO₃)-COOH); a trendline is included for all compounds. (D) The optical stability of Cy5-(P0₁₀₁₋₁₂₅)₂, Cy5-P0₁₀₁₋₁₂₅, and of corresponding free dyes determined over the course of 30 min (means were fitted).

The stacking behavior of Cy5-(P0₁₀₁₋₁₂₅)₂ proved to be similar to that of the free dye COOH-(SO₃)Cy5(SO₃)-COOH at the same concentration (Figure 2B). Conversely, mono-labeled Cy5-P0₁₀₁₋₁₂₅ yielded a higher “shoulder peak”, which is indicative for dye stacking [28].

Increase in temperature, with a resulting enhancement of the structural mobility in the bridging Cy5 dye, yielded a 65% loss of fluorescence intensity for a dimer and slightly more for a monomer (70%), while for the symmetrical free dye COOH-(SO₃)Cy5(SO₃)-COOH a loss in intensity of about 80% was seen (Figure 2C).

2.3. P0 Binding Affinity and Cellular Fluorescence Intensity

RT4-D12 Schwannoma cells were selected for in vitro experiments based on their origin and their specific P0-expressing properties [11].

Saturation binding experiments revealed a K_D for Cy5-(P0₁₀₁₋₁₂₅)₂ of 70.3 ± 10 nM (Figure 3A), which is a 1.5-fold increase compared to Cy5-P0₁₀₁₋₁₂₅ (K_D : 104.9 ± 16.7 nM; $p = 0.003$). Nonspecific binding was comparable for both tracers (0.020 for Cy5-P0₁₀₁₋₁₂₅ and 0.022 for Cy5-(P0₁₀₁₋₁₂₅)₂). Quantification of the fluorescence intensity in flow-cytometry studies performed with a tracer concentration range between 5 and 1000 nM demonstrated a concentration-dependent signal intensity for both tracers (Figure 3B). On average, at the same concentration, a 44% higher (range 34–59%; Figure 3B) fluorescence signal intensity was seen for Cy5-(P0₁₀₁₋₁₂₅)₂ compared to the fluorescence signal intensity of Cy5-P0₁₀₁₋₁₂₅

($p < 0.00001$). As a result, the bench mark signal intensity for Cy5-P0₁₀₁₋₁₂₅ at 1 mM [11] was comparable to the signal intensity seen for Cy5-(P0₁₀₁₋₁₂₅)₂, between 250–100 nM (Figure 3B), yielding about a 4-fold increase in staining efficiency.

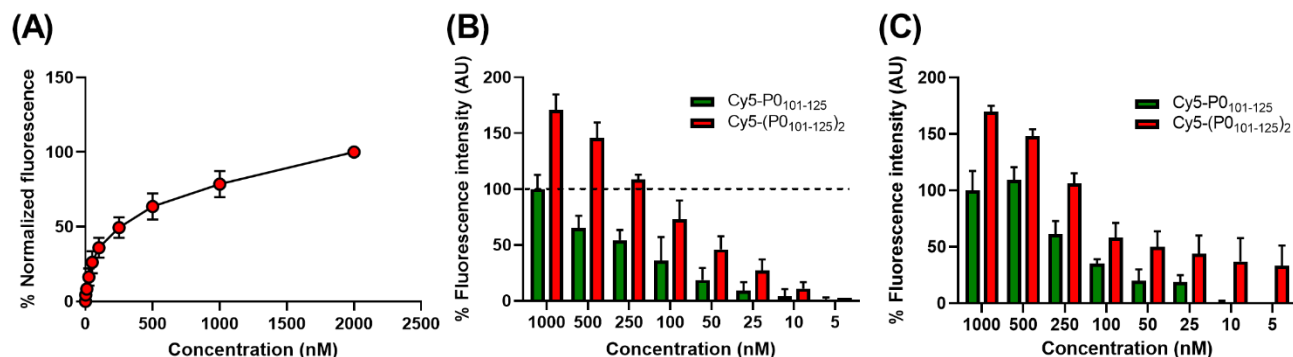


Figure 3. Quantified assessment of binding affinity and signal intensity. (A) Saturation binding curve for Cy5-(P0₁₀₁₋₁₂₅)₂ as determined using flow cytometry after incubation of cells with increasing tracer concentrations (0–2000 nM). (B) Quantification via flow cytometry and (C) via fluorescence confocal microscopy of the fluorescence intensity per cell for Cy5-P0₁₀₁₋₁₂₅ (green bars) and Cy5-(P0₁₀₁₋₁₂₅)₂ (red bars) at different tracer concentrations.

Fluorescence confocal microscopy of cultured Schwannoma cells confirmed P0 targeting and underscores the concentration-dependent staining observed with flow cytometry (Figures 3C and 4), where cells could be clearly discriminated based on their P0 expression at using 100nM Cy5-(P0₁₀₁₋₁₂₅)₂. Only a faint P0-related signal could be detected after incubation of Cy5-P0₁₀₁₋₁₂₅ at the same concentration. Cy5-(P0₁₀₁₋₁₂₅)₂ allowed effective visualization of P0 expression at a concentration as low as 10nM, and the signal could be detected down to 5 nM.

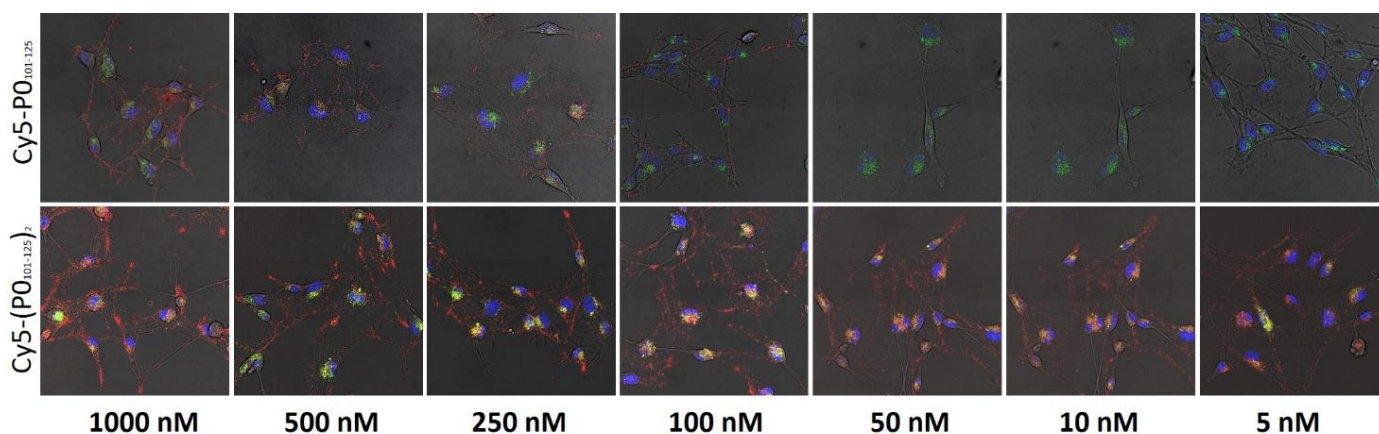


Figure 4. In vitro comparison of Cy5-P0₁₀₁₋₁₂₅ and Cy5-(P0₁₀₁₋₁₂₅)₂. Fluorescence confocal imaging of P0-expressing RT4-D12 Schwannoma cells after incubation with different concentrations of either Cy5-P0₁₀₁₋₁₂₅ or Cy5-(P0₁₀₁₋₁₂₅)₂ (5–1000 nM). P0 tracer in red, lysosomes in green, and nucleus in blue.

3. Discussion

By synthesizing Cy5-(P0₁₀₁₋₁₂₅)₂, we were able to create a dimeric imaging agent that has a superior affinity for P0 and more effectively stains cellular P0, thereby taking yet another step forwards in the realization of successful intraoperative nerve illumination.

As stated in the introduction, multimerization is commonly employed to increase binding affinity [18,29]. While there was no discernible difference in nonspecific binding for mono- and bi-protein-labeled compounds, we found that the presence of two targeting

vectors on a single tracer boosted the K_D to 70.3 ± 10.0 nM, converting to a 1.5-fold gain in receptor affinity compared to Cy5-P0_{101–125}. This is a rise that is in line with previous reports mentioning peptide multimers [24,29]. Having an additional P0_{101–125} moiety also shields the Cy5 dye from serum interactions (Table 1), thereby lowering the serum binding by more than 20%. As serum binding of imaging agents makes for a notorious cause of background staining [30] and drives hepatic uptake/clearance [31], such a reduction supports more favorable pharmacokinetics. Finally, we found that the dimerization improved the optical properties of the nerve tracer by preventing dye stacking (see Figure 2A,B).

While comparing concentration dependence on stacking behavior of both protein-conjugated compounds (Figure S4A,B) we observed that a typical “stacking shoulder” appears only for a mono-labeled Cy5-P0_{101–125} at higher concentration. This indicates that P0_{101–125} moieties in the mono-substituted compound, at higher concentrations, aggregate with other monomers, thus bringing dyes in close vicinity of each other and causing a typical “dye-dye stacking” peak to occur in the absorbance spectrum (see Figure 2A) [27]. Conversely, addition of a second P0_{101–125} prevents such interactions from occurring.

Overall, Cy5-(P0_{101–125})₂ was able to effectively stain cellular P0 at 4-fold lower concentrations compared to the mono-substituted compound, meaning it was effective at a lower dye-to-peptide ratio.

Despite the potential clinical benefit of nerve imaging, it has proved challenging to create nerve-specific imaging tracers. While various preclinical studies show promising results [32], there are a number of risks holding back the translation of these approaches. Hereby, toxicity is a major concern. Specifically, long-term toxic effects of nerve targeting tracers could ultimately do more harm than good, meaning the resulting complications could be worse than the complications that are avoided by providing a nerve-sparing surgical procedure. Using P0_{101–125} has as advantage that the central nervous system is not affected [11], and one can argue that the potential dose reduction (see Figures 3 and 4) also helps reduce the chance of toxic effects, especially when combined with local injections [33]. More extensive in vivo studies are, however, needed to corroborate this.

4. Materials and Methods

All chemicals were received from Actu-All Chemical (Oss, The Netherlands), Sigma Aldrich (St. Louis, MO, USA), Tokyo Chemical Industry (Tokyo, Japan), Biosolve BV (Valkenswaard, The Netherlands), VWR Chemicals (Solon, OH, USA) and used without further purification. DMF and DMSO were dried over four Å molecular sieves at least for 24 h prior to use. Preparative high-pressure liquid chromatography (prep-HPLC) was performed on a Waters HPLC system (Waters Chromatography B.V., Etten-Leur, The Netherlands) using a 2545 quaternary gradient module pump and a 2489 UV detector. Dr. Maisch ReproSil-Pur 120 C18-AQ 10 µM (250 mm × 20 mm) column (Dr. Maisch HPLC GmbH, Ammerbuch-Entringen, Germany) was applied operating flow rate of 12 mL/min. HPLC analysis was carried out on Waters Alliance 2690 using a Waters symmetry C₁₈ column (2.1 × 150 mm) with a gradient of 0.1% TFA in H₂O/MeCN 95:5 to 0.1% TFA in H₂O/MeCN 5:95 in 17 min (0.3 mL/min). Mass spectrometry was performed on a Microflex LT/SH MALDI-TOF mass spectrometer (Bruker, Billerica, MA, USA). Lyophilization was performed with a VaCo 2-II lyophilizer (Zirbus technology GmbH, Bad Grund (Harz), Germany). Absorption spectrometry was performed using a UV1280 UV-vis spectrometer (Shimadzu, Kyoto, Japan), and fluorescence spectrometry was performed using an LS55 (Perkin Elmer, Waltham, MA, USA). The fluorescence spectra at different temperatures were measured on an Agilent Cary Eclipse (Agilent Cary Eclipse, Santa Clara, CA, USA). NMR spectra were measured on a Bruker Avance 300 (Bruker, Billerica, MA, USA) operating at 300 MHz for ¹H and 75.00 MHz for ¹³C, using the residual solvents (CDCl₃ and DMSO-d₆) as internal references, and on a Bruker Avance III spectrometer operating at 600 MHz for ¹H and equipped with a 2.5 mm PH SEI probe (Bruker, Billerica, MA, USA). For photostability, a prototype D-Light P surgical laparoscope (KARL STORZ, Tuttlingen,

Germany) was used. Fluorescence confocal imaging was performed using a SP8 WLL confocal microscope (Leica Microsystems, Wetzlar, Germany). Obtained images were analyzed using Leica Confocal Software (Leica Microsystems). Mean fluorescence intensity values per sample were measured using a LSRII flow cytometer (BD Biosciences, Franklin Lakes, NJ, USA) with APC-A settings (635 nm laser and 750 nm long-pass filter). The binding constant (K_D) of the normalized geometric means were fitted with equations in the Prism 5 software (GraphPad, San Diego, CA, USA). Statistical evaluation (Student's *t*-test) for all properties was performed in the Prism 5 software. Figure 1 was created using BioRender (<https://biorender.com/>, accessed on 7 October 2022).

4.1. Synthetic Procedures

Peptide P0_{101–125} (Ac-KNPPDIVGKTSQVTLYVFEKVPTRYC-NH₂), Sulfonate-(SO₃)Cy5(SO₃)-Maleimide, and Cy5-P0_{101–125} were synthesized following a procedure previously reported by Buckle et al. [11].

Maleimide-(SO₃)Cy5(SO₃)-Maleimide (1) and Cy5-(P0_{101–125})₂ (2) were synthesized by slightly adapting procedures reported before in the literature [11].

Synthesis of 1. First, 46 mg of HOOC-(SO₃)Cy5(SO₃)-COOH [27] (62 μmol) was dissolved in DMF (3 mL), followed by addition of *N*-(2-aminoethyl)maleimide trifluoroacetate salt (39 mg, 155 μmol) and PyBOP (12.9 mg, 24.7 μmol). To this mixture, *N*-methyl morpholine (54.5 μL, 495 μmol) was added, and the reaction mixture was stirred at room temperature (r.t.) for 2 h. The reaction mixture was subsequently acidified with trifluoroacetic acid (TFA) (50 μL) and purified using preparative HPLC, employing a gradient of 5–95% acetonitrile over 51 min. Lyophilization of product-containing fractions yielded the title compound as a dark blue solid (40.3 mg, 40.78 μmol, 66 % isolated yield). MALDI-TOF [C₄₉H₅₇N₆O₁₂S₂²⁻ + 2H]⁺ calculated 988.2, found 988.3. ¹H NMR (300 MHz, MeOD) δ 8.30 (dd, *J* = 17.0, 9.0 Hz, 2 H), 7.89 (s, 3 H), 7.87 (d, *J* = 1.4 Hz, 1 H), 7.35 (t, *J* = 7.7 Hz, 2 H), 6.80 (s, 4 H), 6.68 (t, *J* = 12.4 Hz, 1 H), 6.36 (d, *J* = 13.7 Hz, 2 H), 4.13 (t, *J* = 7.0 Hz, 4 H), 3.60 (dd, *J* = 6.4, 4.5 Hz, 4 H), 3.35 (dd, *J* = 6.4, 4.6 Hz, 4 H), 2.13 (t, *J* = 7.2 Hz, 4 H), 1.81 (dt, *J* = 11.6, 5.9 Hz, 4 H), 1.75 (s, 12 H), 1.64 (dt, *J* = 14.7, 7.2 Hz, 5 H), 1.52–1.37 (m, 4H), 1.31 (t, *J* = 7.4 Hz, 1 H). ¹³C NMR (75 MHz, MeOD) δ 174.81, 173.92, 171.17, 154.72, 143.53, 142.01, 141.24, 134.10, 126.68, 119.96, 110.32, 103.94, 53.41, 49.20, 49.17, 48.46, 48.17, 47.89, 47.61, 47.32, 47.04, 46.75, 43.66, 37.51, 37.10, 35.11, 26.71, 26.45, 25.83, 24.83.

Synthesis of 2. Maleimide-(SO₃)Cy5(SO₃)-Maleimide (1) (6 mg, 6 μmol) and P0_{101–125} (Ac-KNPPDIVGKTSQVTLYVFEKVPTRYC-NH₂; 45 mg, 15 μmol) were dissolved in a mixture of phosphate-buffered saline (PBS) (5 mL; pH 7.4) and DMF (1 mL) and allowed to react at r.t. for 2 h. The reaction mixture was diluted with water and acetonitrile. The crude product was purified from side products of the reaction and excess of the free peptide by preparative HPLC employing a gradient of (25–95% acetonitrile in 30 min) to yield the title compound as a light blue solid (25.3 mg, 35.8 μmol, 67% isolated yield). A 58 μM stock in Milli-Q was prepared for use in further experiments. MALDI-TOF [C₃₂₅H₄₉₃N₇₄O₉₂S₄⁴⁻ + Na]⁺; calculated 7035.2, found 7035.8.

4.2. Chemical Stability

For the stability towards glutathione, which is used as a measure of stability towards thiols and amines in vivo, 125 μL of a 2 mM solution of the compound in (0.1 M HEPES pH 7.4, pre-sparged with N₂) was added to 125 μL of a 4 mM solution of reduced glutathione in 0.1M HEPES pH 7.4 (pre-sparged with N₂). The solutions were mixed and then placed in a sample manager. A sample was analyzed at 37 degrees over 6 h in total to determine the amount of compound relative to *t* = 0.

4.3. Photophysical Properties

The molar extinction coefficient (ϵ), quantum yield (QY), brightness, lipophilicity, serum protein binding, photo- and chemical stability, and stacking behavior were de-

terminated according to a slight modification of the protocol put forward by Hensbergen et al. [34]. Sulfonate-(SO₃)Cy5(SO₃)-COOH [27] was measured and used as a control for QY.

To determine the effect that temperature (range 5 to 65 °C) has on the fluorescence intensity, samples with a maximum absorption of 0.1 AU. were used. Samples were stirred during the measurements and were left to equilibrate after the fluorescence spectrometer reached the right temperature.

To determine the stacking behavior of the mono- and bi-labeled compounds and their corresponding dyes, a dilution series of Cy5-(P₀₁₀₁₋₁₂₅)₂ and Cy5-P₀₁₀₁₋₁₂₅ were made, consisting of the dye concentrations ranging from 8 μM to 0.5 μM.

4.4. Photostability

For photostability measurements, the cuvettes were sealed and illuminated for 5 min (30 min in total) by a modified Storz D-Light P fluorescence imaging system [11] at a distance of 50 mm in a dark environment. After each illumination cycle, the fluorescence intensity was determined.

4.5. Fluorescence Confocal Microscopy

RT4-D12 Schwannoma cells were trypsinized and seeded onto 35 mm culture dishes that contained a glass insert (MatTek co, Emu Plains, New South Wales, Australia) two days prior to the imaging experiment. Then, 0.5–1000 nM Cy5-P₀₁₀₁₋₁₂₅ or Cy5-(P₀₁₀₁₋₁₂₅)₂ was added one hour prior to imaging (incubation at 4 °C; *n* = 3 per tracer). Peptide solutions were sonicated for 20 s prior to addition to prevent aggregation of the peptide in solution. LysoTracker (lysotracker green; 2 μL/mL DND-26, Thermo Fisher, Waltham, MA, USA) and Hoechst (33,342, 1 mg/mL, 1:500, Thermo Fisher) were added to the to provide staining of lysosomes and the nucleus, respectively.

Images were acquired following Cy5 excitation at 633 nm. Emission was collected between 650–700 nm. For visualization of the lysosomes in the cells, a 488 nm laser was used for excitation, while emission was collected between 500–550 nm. Hoechst was excited at 405 nm, and emission was collected between 410–460 nm. Fluorescence confocal images were acquired using a Leica SP8 WL at sequential settings and 63× magnification. Image analysis was performed using Leica Confocal Software (Leica Microsystems). Semi-quantitative analysis of the Cy5 signal intensity was performed using the quantification tool in Fiji software according to previously described methods [35,36].

4.6. Flow Cytometry

Flow cytometric analysis was performed using RT4-D12 Schwannoma cells after incubation with either Cy5-P₀₁₀₁₋₁₂₅ or Cy5-(P₀₁₀₁₋₁₂₅)₂. For saturation binding experiments, Cy5-labelled peptides were added to the cell samples in a range of 0–2000 nM in 50 μL of 0.1% bovine serum albumin (BSA) in PBS, as previously described [11,17]. After 1 h of incubation at 4 °C, the cells were washed two times with 300 μL of 0.1% BSA in PBS and re-suspended in 300 μL of 0.1% BSA. Cells were gated on Forward Scatter and Side Scatter, and a minimum of 10,000 viable cells were analyzed per sample. All experiments were performed in triplicate.

For evaluation of the differences in signal intensity per concentration between Cy5-P₀₁₀₁₋₁₂₅ and Cy5-(P₀₁₀₁₋₁₂₅)₂ (5–1000 nM), the mean signal intensity of Cy5-P₀₁₀₁₋₁₂₅ at 1000nM was set at 100%, and intensities measured at other tracer concentrations or for Cy5-(P₀₁₀₁₋₁₂₅)₂ were calculated as % increase or decrease from this point. The K_D values of the evaluated peptides were calculated using the “Binding-Saturation, One site—Total” nonlinear regression equation, as described previously [17].

4.7. Statistical Evaluation

Statistical evaluation for comparison of the photophysical properties (brightness, photostability), chemical properties (lipophilicity), K_D, and fluorescence signal intensity values were performed using unpaired Student's *t*-test comparing the means between

Cy5-P0_{101–125} and Cy5-(P0_{101–125})₂, where Cy5-P0_{101–125} is a control group. Value $p < 0.05$ are considering as a significant.

Normalization of the data set for stacking behavior was performed using Equation (1):

$$x(\text{normalized}) = \frac{(x - x_{\min})}{\text{range of } x} \quad (1)$$

where range of $x = x_{\max} - x_{\min}$.

5. Conclusions

Our findings indicate that Cy5-(P0_{101–125})₂ has a superior affinity for P0, which led to 4-fold increase in efficiency compared to Cy5-P0_{101–125}. Therefore, dimerization provides a feasible means to advance P0-specific nerve imaging strategies.

6. Patents

European patent application No.16180535.3.

Supplementary Materials: The following supporting information can be downloaded at <https://www.mdpi.com/article/10.3390/molecules27249015/s1>, Figure S1: NMR characterization of maleimide-(SO₃)Cy5(SO₃)-maleimide (1). (A) ¹H NMR spectra (300 MHz, MeOD); (B) ¹³C NMR spectra (75 MHz, MeOD); Figure S2: MALDI-TOF mass spectra of (A) maleimide-(SO₃)Cy5(SO₃)-maleimide (1) and (B) Cy5-(P0_{101–125})₂ (2); Figure S3: ¹H NMR spectra of (A) Cy5-P0_{101–125} (600 MHz, D₂O), (B) Cy5-(P0_{101–125})₂ (600 MHz, D₂O), (C) Cy5-(P0_{101–125})₂ (600 MHz, DMSO); Figure S4: Concentration-dependent stacking behavior of Cy5-P0_{101–125} and Cy5-(P0_{101–125})₂ and corresponding free dyes measured in H₂O.

Author Contributions: Conceptualization, N.B., T.B. and F.W.B.v.L.; methodology N.B., T.B., M.P.v.M., A.B., A.H.V. and F.W.B.v.L.; validation, N.B., T.B., M.P.v.M. and F.W.B.v.L.; formal analysis, N.B., T.B., M.P.v.M., A.B., A.H.V. and F.W.B.v.L.; investigation, N.B., T.B., M.P.v.M. and A.B.; resources, A.H.V. and F.W.B.v.L.; data curation, N.B., T.B., M.P.v.M. and A.B.; writing—original draft preparation, N.B., T.B. and F.W.B.v.L.; visualization, N.B., T.B. and F.W.B.v.L.; writing—review and editing, N.B., T.B., M.P.v.M., A.B., A.H.V. and F.W.B.v.L.; supervision, T.B. and F.W.B.v.L.; project administration, T.B.; funding acquisition, F.W.B.v.L. All authors have read and agreed to the published version of the manuscript.

Funding: This research was funded by the Research Foundation of Flanders (Grant no. FWO S000922N) and a NWO-TTW-VICI (TTW BGT16141) grant supported by the Dutch Research Council.

Institutional Review Board Statement: Not applicable.

Informed Consent Statement: Not applicable.

Data Availability Statement: The data presented in this study are available on request from the corresponding author. The data are not publicly available due to patent restrictions.

Acknowledgments: We thank Danny van Willigen, Fabian Hensbergen and Romy van Leeuwen for their assistance.

Conflicts of Interest: The authors declare no conflict of interest.

Sample Availability: Samples of the compounds Cy5-P0_{101–125} and Cy5-(P0_{101–125})₂ (including non-functionalized peptides and dye components) are available from the authors.

References

1. Menorca, R.M.G.; Fussell, T.S.; Elfar, J.C. Nerve Physiology Mechanisms of Injury and Recovery. *Hand Clin.* **2013**, *29*, 317–330. [[CrossRef](#)] [[PubMed](#)]
2. Moszkowicz, D.; Alsaïd, B.; Bessedé, T.; Penna, C.; Nordlinger, B.; Benoit, G.; Peschard, F. Where does pelvic nerve injury occur during rectal surgery for cancer? *Color. Dis.* **2011**, *13*, 1326–1334. [[CrossRef](#)] [[PubMed](#)]
3. Daniels, I.R.; Woodward, S.; Taylor, F.G.; Raja, A.; Toomey, P. Female urogenital dysfunction following total mesorectal excision for rectal cancer. *World J. Surg. Oncol.* **2006**, *4*, 6. [[CrossRef](#)]

4. Clausen, N.; Wolloscheck, T.; Konerding, M.A. How to optimize autonomic nerve preservation in total mesorectal excision: Clinical topography and morphology of pelvic nerves and fasciae. *World J. Surg.* **2008**, *32*, 1768–1775. [[CrossRef](#)]
5. Lee, Y.H.; Huang, J.K.; Lu, C.M. The impact on sexual function after nerve sparing and non-nerve sparing radical retropubic prostatectomy. *J. Chin. Med. Assoc.* **2003**, *66*, 13–18.
6. Noldus, J.; Michl, U.; Graefen, M.; Haese, A.; Hammerer, P.; Huland, H. Patient-reported sexual function after nerve-sparing radical retropubic prostatectomy. *Eur. Urol.* **2002**, *42*, 118–124. [[CrossRef](#)]
7. Walsh, E.M.; Cole, D.; Tipirneni, K.E.; Bland, K.I.; Udayakumar, N.; Kasten, B.B.; Bevans, S.L.; McGrew, B.M.; Kain, J.J.; Nguyen, Q.T.; et al. Fluorescence Imaging of Nerves During Surgery. *Ann. Surg.* **2019**, *270*, 69–76. [[CrossRef](#)]
8. Lu, J. Neuronal tracing for connectomic studies. *Neuroinformatics* **2011**, *9*, 159–166. [[CrossRef](#)]
9. Cotero, V.E.; Siclovan, T.; Zhang, R.; Carter, R.L.; Bajaj, A.; LaPlante, N.E.; Kim, E.; Gray, D.; Staudinger, V.P.; Yazdanfar, S.; et al. Intraoperative fluorescence imaging of peripheral and central nerves through a myelin-selective contrast agent. *Mol. Imaging Biol.* **2012**, *14*, 708–717. [[CrossRef](#)]
10. Park, M.H.; Hyun, H.; Ashitate, Y.; Wada, H.; Park, G.; Lee, J.H.; Njiojob, C.; Henary, M.; Frangioni, J.V.; Choi, H.S. Prototype Nerve-Specific Near-Infrared Fluorophores. *Theranostics* **2014**, *4*, 823–833. [[CrossRef](#)]
11. Buckle, T.; Hensbergen, A.W.; van Willigen, D.M.; Bosse, F.; Bauwens, K.; Pelger, R.C.M.; van Leeuwen, F.W.B. Intraoperative visualization of nerves using a myelin protein-zero specific fluorescent tracer. *EJNMMI Res.* **2021**, *11*, 50. [[CrossRef](#)] [[PubMed](#)]
12. Zheng, L.; Li, K.; Han, Y.; Wei, W.; Zheng, S.; Zhang, G. In vivo targeted peripheral nerve imaging with a nerve-specific nanoscale magnetic resonance probe. *Med. Hypotheses* **2014**, *83*, 588–592. [[CrossRef](#)] [[PubMed](#)]
13. Azargoshasb, S.; Boekestijn, I.; Roestenberg, M.; KleinJan, G.H.; van der Hage, J.A.; van der Poel, H.G.; Rietbergen, D.D.D.; van Oosterom, M.N.; van Leeuwen, F.W.B. Quantifying the Impact of Signal-to-background Ratios on Surgical Discrimination of Fluorescent Lesions. *Mol. Imaging Biol.* **2022**. [[CrossRef](#)] [[PubMed](#)]
14. Huskens, J. Multivalent interactions at interfaces. *Curr. Opin. Chem. Biol.* **2006**, *10*, 537–543. [[CrossRef](#)] [[PubMed](#)]
15. Kiessling, L.L.; Gestwicki, J.E.; Strong, L.E. Synthetic multivalent ligands as probes of signal transduction. *Angew. Chem. Int. Ed. Engl.* **2006**, *45*, 2348–2368. [[CrossRef](#)]
16. Gonzalez-Cuesta, M.; Ortiz Mellet, C.; Garcia Fernandez, J.M. Carbohydrate supramolecular chemistry: Beyond the multivalent effect. *Chem. Commun. (Camb.)* **2020**, *56*, 5207–5222. [[CrossRef](#)]
17. Kuil, J.; Buckle, T.; Yuan, H.; van den Berg, N.S.; Oishi, S.; Fujii, N.; Josephson, L.; van Leeuwen, F.W. Synthesis and evaluation of a bimodal CXCR4 antagonistic peptide. *Bioconjug. Chem.* **2011**, *22*, 859–864. [[CrossRef](#)]
18. Chittasupho, C. Multivalent ligand: Design principle for targeted therapeutic delivery approach. *Ther. Deliv.* **2012**, *3*, 1171–1187. [[CrossRef](#)]
19. Kwon, Y.D.; Chung, H.J.; Lee, S.J.; Lee, S.H.; Jeong, B.H.; Kim, H.K. Synthesis of novel multivalent fluorescent inhibitors with high affinity to prostate cancer and their biological evaluation. *Bioorg. Med. Chem. Lett.* **2018**, *28*, 572–576. [[CrossRef](#)]
20. Bohmer, V.I.; Szymanski, W.; Feringa, B.L.; Elsinga, P.H. Multivalent Probes in Molecular Imaging: Reality or Future? *Trends Mol. Med.* **2021**, *27*, 379–393. [[CrossRef](#)]
21. Liu, W.; Hao, G.; Long, M.A.; Anthony, T.; Hsieh, J.T.; Sun, X. Imparting multivalency to a bifunctional chelator: A scaffold design for targeted PET imaging probes. *Angew. Chem. Int. Ed. Engl.* **2009**, *48*, 7346–7349. [[CrossRef](#)] [[PubMed](#)]
22. Cho, H.J.; Huynh, T.T.; Rogers, B.E.; Mirica, L.M. Design of a multivalent bifunctional chelator for diagnostic (64)Cu PET imaging in Alzheimer's disease. *Proc. Natl. Acad. Sci. USA* **2020**, *117*, 30928–30933. [[CrossRef](#)] [[PubMed](#)]
23. Kuil, J.; Velders, A.H.; van Leeuwen, F.W. Multimodal tumor-targeting peptides functionalized with both a radio- and a fluorescent label. *Bioconjug. Chem.* **2010**, *21*, 1709–1719. [[CrossRef](#)] [[PubMed](#)]
24. Yeldell, S.B.; Seitz, O. Nucleic acid constructs for the interrogation of multivalent protein interactions. *Chem. Soc. Rev.* **2020**, *49*, 6848–6865. [[CrossRef](#)]
25. Li, D.H.; Schreiber, C.L.; Smith, B.D. Sterically Shielded Heptamethine Cyanine Dyes for Bioconjugation and High Performance Near-Infrared Fluorescence Imaging. *Angew. Chem. Int. Ed. Engl.* **2020**, *59*, 12154–12161. [[CrossRef](#)]
26. Ptaszek, M. Rational design of fluorophores for in vivo applications. *Prog. Mol. Biol. Transl. Sci.* **2013**, *113*, 59–108. [[CrossRef](#)]
27. Spa, S.J.; Hensbergen, A.W.; van der Wal, S.; Kuil, J.; van Leeuwen, F.W.B. The influence of systematic structure alterations on the photophysical properties and conjugation characteristics of asymmetric cyanine 5 dyes. *Dyes Pigments* **2018**, *152*, 19–28. [[CrossRef](#)]
28. van der Wal, S.; Kuil, J.; Valentijn, A.R.P.M.; van Leeuwen, F.W.B. Synthesis and systematic evaluation of symmetric sulfonated centrally C-C bonded cyanine near-infrared dyes for protein labelling. *Dyes Pigments* **2016**, *132*, 7–19. [[CrossRef](#)]
29. Kuil, J.; Buckle, T.; Oldenburg, J.; Yuan, H.; Borowsky, A.D.; Josephson, L.; van Leeuwen, F.W. Hybrid peptide dendrimers for imaging of chemokine receptor 4 (CXCR4) expression. *Mol. Pharm.* **2011**, *8*, 2444–2453. [[CrossRef](#)]
30. Berezin, M.Y.; Guo, K.; Akers, W.; Livingston, J.; Solomon, M.; Lee, H.; Liang, K.; Agee, A.; Achilefu, S. Rational approach to select small peptide molecular probes labeled with fluorescent cyanine dyes for in vivo optical imaging. *Biochemistry* **2011**, *50*, 2691–2700. [[CrossRef](#)]
31. Gibbs, S.L. Near infrared fluorescence for image-guided surgery. *Quant. Imaging Med. Surg.* **2012**, *2*, 177–187. [[CrossRef](#)] [[PubMed](#)]

32. Gibbs-Strauss, S.L.; Nasr, K.A.; Fish, K.M.; Khullar, O.; Ashitate, Y.; Siclovan, T.M.; Johnson, B.F.; Barnhardt, N.E.; Hehir, C.A.T.; Frangioni, J.V. Nerve-Highlighting Fluorescent Contrast Agents for Image-Guided Surgery. *Mol. Imaging* **2011**, *10*, 91–101. [[CrossRef](#)] [[PubMed](#)]
33. Wang, L.G.; Barth, C.W.; Kitts, C.H.; Mebrat, M.D.; Montano, A.R.; House, B.J.; McCoy, M.E.; Antaris, A.L.; Galvis, S.N.; McDowall, I.; et al. Near-infrared nerve-binding fluorophores for buried nerve tissue imaging. *Sci. Transl. Med.* **2020**, *12*, eaay0712. [[CrossRef](#)]
34. Hensbergen, A.W.; Buckle, T.; van Willigen, D.M.; Schottelius, M.; Welling, M.M.; van der Wijk, F.A.; Maurer, T.; van der Poel, H.G.; van der Pluijm, G.; van Weerden, W.M.; et al. Hybrid Tracers Based on Cyanine Backbones Targeting Prostate-Specific Membrane Antigen: Tuning Pharmacokinetic Properties and Exploring Dye-Protein Interaction. *J. Nucl. Med.* **2020**, *61*, 234–241. [[CrossRef](#)]
35. Buckle, T.; van der Wal, S.; van Willigen, D.M.; Aalderink, G.; KleinJan, G.H.; van Leeuwen, F.W.B. Fluorescence background quenching as a means to increase Signal to Background ratio—A proof of concept during Nerve Imaging. *Theranostics* **2020**, *10*, 9890–9898. [[CrossRef](#)]
36. Van der Wal, S.; de Korne, C.M.; Sand, L.G.L.; van Willigen, D.M.; Hogendoorn, P.C.W.; Szuhai, K.; van Leeuwen, F.W.B.; Buckle, T. Bioorthogonally Applicable Fluorescence Deactivation Strategy for Receptor Kinetics Study and Theranostic Pretargeting Approaches. *ChemBioChem* **2018**, *19*, 1758–1765. [[CrossRef](#)]